Spectroscopic diagnostics in a colliding-blast-wave experiment

R. C. Elton,* D.-M. Billings, C. K. Manka, H. R. Griem,* J. Grun, and B. H. Ripin
Plasma Physics Division, Naval Research Laboratory, Washington, D.C. 20375

J. Resnick
Research Support Instruments, Inc., Alexandria, Virginia 22314
(Received 29 April 1993)

Visible spectral lines from $n=3$, $\Delta n=0$ transitions in N^+ and N^{2+} ions are used for measuring the plasma electron density and temperature in a region of two colliding blast waves, propagating through a 1.5–10-Torr nitrogen atmosphere. The blast waves originate at the tips of two aluminum rods irradiated with two beams of the Naval Research Laboratory (NRL) Pharos-III 1.054-μm-wavelength Nd:glass laser operated at an energy of 200–430 J for each beam in 5-ns pulses. An electron density in the colliding-blast-wave region of $N_e \approx 10^{18}$ cm^{-3} was deduced from Stark broadening of spectral lines from N^+ ions. An electron temperature of $T_e \approx 4$ eV was measured in this region from a spectral-line intensity ratio between N^{2+} and N^+ ions. Near one target, an electron density of $N_e \approx 8\times 10^{20}$ cm^{-3} was determined from series-limit x-ray spectral-line merging; a mean electron temperature of $kT_e \approx 225$ eV was determined from x-ray line-intensity ratios. Some evidence was found for enhanced velocities for blast waves propagating through a plasma formed by a preceding blast wave.

PACS number(s): 52.25.Nr, 52.25.Rv, 52.35.Tc

I. INTRODUCTION

The study of blast waves created by the interaction of a laser-produced plasma with a low-density gas is important for the understanding of numerous processes in space physics, plasma chemistry, and hydrodynamics [1]. Numerical modeling often has been applied to laboratory experiments and the results compared with detailed diagnostic measurements, in part to verify existing codes. Of expanded interest is the interaction of two intersecting blast waves. Such dual colliding blast waves have been studied in electromagnetic shock tubes, beginning in the 1960s at moderate relative speeds [2], and are expected to produce effects that are different in location, scale, density, temperature, and duration as compared to those of individual blast waves, along with a strong interaction region.

The experiments described here represent an attempt to experimentally study the time dependence of the spectra from colliding and interpenetrating high-Mach-number (>100) blast waves on a laboratory scale [3]. Two laser beams are directed onto aluminum targets, and the resulting plasmas expand into a nitrogen atmosphere at pressures varying from 1.5–10 Torr, in the "collisional" regime [4]. Various diagnostic techniques are used to determine the effects.

In this paper we mainly discuss time-resolved spectroscopic diagnostics of nitrogen ions over a wavelength range of 460–464 nm. From these we deduce the ionic species present, the plasma electron temperature and density, and the shock-front position, all as a function of time after target irradiation and of distance from the target in the vicinity of the expanding and interacting blast waves. The densities derived are compared with interferometric measurements [5].

In addition to these late-time and distant measurements in the visible spectral region, we also obtained values for the initial hot plasma electron density and temperature near the aluminum targets, using x-ray spectroscopic measurements. Such measurements are of considerable interest as initial conditions in a global model of the experiment. We measured the x-ray spectral emission at both targets simultaneously on each shot while incorporating some spatial resolution to determine the limit of expansion of the hot aluminum plasma between the targets.

II. EXPERIMENT

The experiment was performed in a 1.2-m-diam. vacuum chamber, typically evacuated to a pressure of 5×10^{-5} Torr prior to each shot. Two beams from the Pharos III laser system operating at 1.054-μm wavelength were directed into the vacuum chamber after passing through 2.2-m-focal-length lenses. They were focused to a typical diameter of 500 μm onto the ends of two aluminum-rod targets of 2.5-mm diameter separated by 30 mm, as shown in Fig. 1. The laser energy on target varied from 200 to 430 J per beam, and the pulse duration was 5 nsec. Hence the irradiance on target was in the range of $(2-4)10^{13}$ W/cm^2 per beam. The two beams were measured to be simultaneous to within ± 0.5 nsec.

*Also at Dept. of Physics & Astronomy, University of Maryland, College Park, MD 20742.

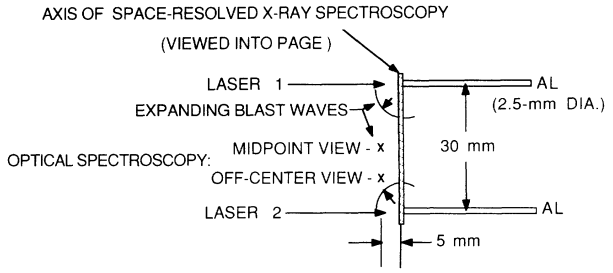

FIG. 1. Schematic of the experiment. Time-resolved optical spectroscopic views are into the page at the points indicated by x's. The x-ray spectrograph viewed the entire aluminum-plasma plumes, while the axis of spatial resolution is shown shaded.

A. Time-resolved visible spectroscopy

A region of plasma of approximately 4 mm in diameter was viewed spectroscopically through a fiber-optics coupling to a 0.5-m focal length Czerny-Turner type spectrometer (Fig. 1). A fast streak camera was attached to the exit port such that its entrance slit was located at the focal plane of the spectrometer. For most of the experiments the streak camera was operated at a speed of 10 μsec/sweep, and an absolute temporal resolution of ≤ 200 nsec was obtained (limited by the entrance slit width). The output of this streak camera was coupled to a charge-coupled device camera. The image obtained was transferred to a computer for storage and data processing. A spectral resolution of <0.05 nm was measured for the system, using a low-pressure xenon lamp. The measured gradients are limited by the field of view and temporal resolution obtained; however, the *relative* differences found for varying wave and viewing conditions are not expected to be affected by such limitations.

As indicated in Fig. 1, the visible spectroscopic measurements were performed at a position 5 mm towards the incoming laser beams and at two positions along the axis between the target tips, namely, at the "midpoint," in order to observe the collision of two equal blast waves, and "off center" at either 7.5 or 10 mm from one target ($\frac{1}{4}$ or $\frac{1}{3}$ the total 30-mm separation, respectively), in order to observe the interpenetration and/or reflection (or collision followed by regeneration) of one blast front with the other. Both single- as well as dual-laser plasma experiments were performed with one and two beams, respectively.

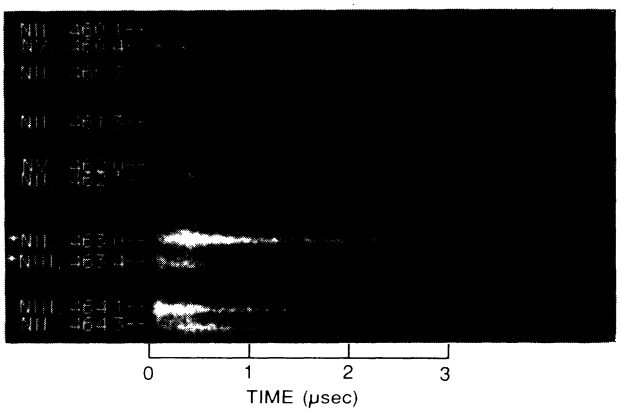

FIG. 2. Sample visible spectrum for the same dual-plasma shot as analyzed in Fig. 3, case (c), viewing off-center at 7.5 mm from the nearer target. N II spectral lines originate from N^+ nitrogen ions, etc. The wavelengths are indicated in nanometers. Asterisks denote two major lines analyzed for electron density and temperature. Time is measured here from the start of the spectral luminosity, not from that of target irradiation.

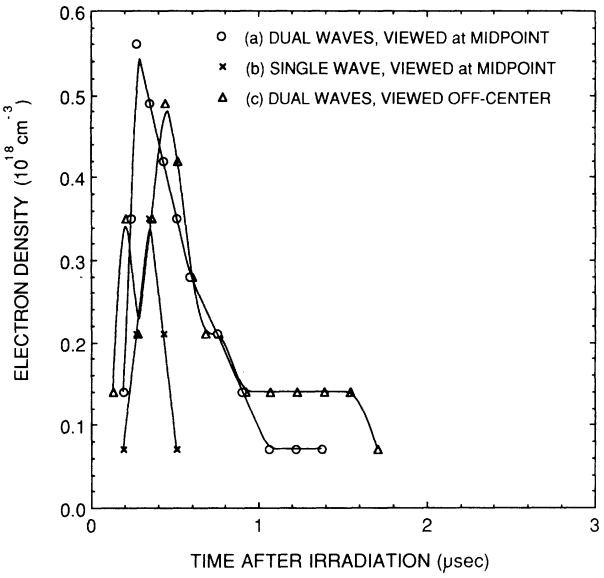

FIG. 3. Electron density in the blast-wave region vs time after target irradiation for three conditions and for a nitrogen fill pressure of 1.5 Torr. Same shot as shown in Fig. 2. For case (c), the viewing position is 7.5 mm from the nearer target.

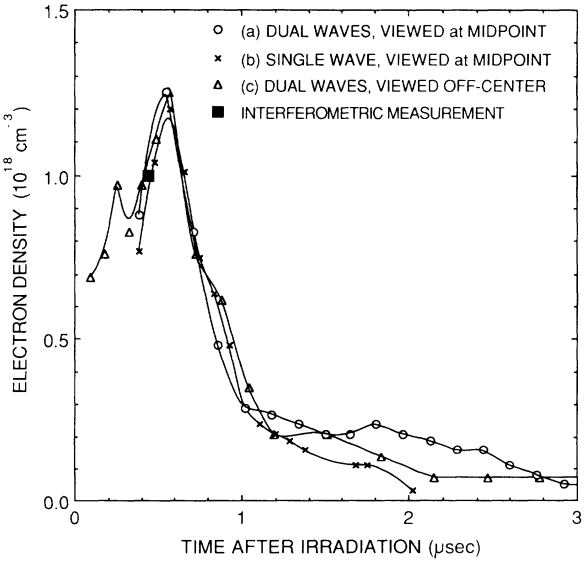

FIG. 4. Electron density in the blast-wave region vs time after target irradiation for three conditions and for a nitrogen fill pressure of 5 Torr. For case (c), the viewing position is 7.5 mm from the nearer target.

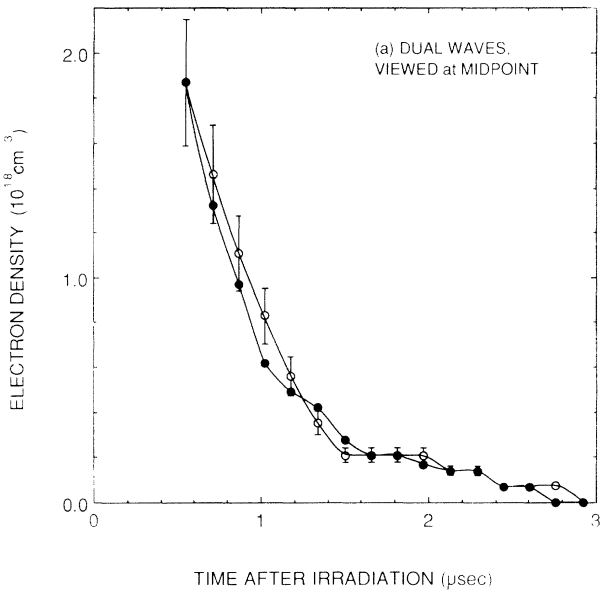

FIG. 5. Electron density in the blast-wave region vs time after target irradiation for a nitrogen fill pressure of 10 Torr and for two successive shots. This is case (a), i.e., dual colliding blast waves viewed at the midpoint between targets. Good reproducibility and experimental uncertainties in the relative density of ±15% are shown.

B. X-ray spectrography

Time-integrated x-ray emission spectra from the plasma were recorded on Kodak direct-exposure film (DEF) using a slitless bent-mica crystal spectrograph that covered the wavelength range of 0.4–1.6 nm (0.8–3 keV photon energy). This spectrograph viewed the plasmas in a direction tangent to the target surfaces, i.e., into the page in Fig. 1. The entrance was located 30 cm from the

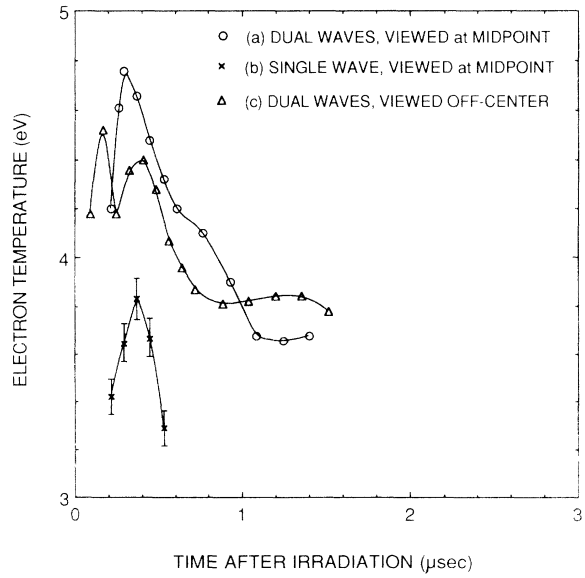

FIG. 6. Electron temperature in the blast-wave region vs time after target irradiation for three conditions and for a nitrogen fill pressure of 1.5 Torr. For case (c), the viewing position is 10 mm from the nearer target.

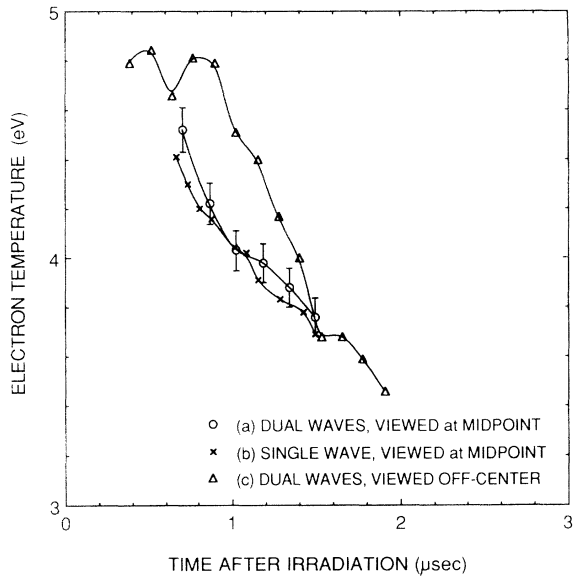

FIG. 7. Electron temperature in the blast-wave region vs time after target irradiation for three conditions and for a nitrogen fill pressure of 5 Torr. For case (c), the viewing position is 7.5 mm from the nearer target.

plasmas. As such, the spectrograph viewed both plasmas expanding from the target tips with some spatial resolution along the axis between them, as indicated by the shaded line in Fig. 1. To obtain such spatial resolution, an entrance slit was installed parallel to the dispersion plane of the spectrograph. This slit was quite wide (1.5–2 mm) in order to obtain adequate intensity for single-shot exposures. The slit width was too large to resolve the x-ray source size itself, but did serve to isolate the two target plasmas on the spectrograms and to show that the hot target plasma did not expand beyond 1–2 mm, i.e., much less than the 30-mm separation. A 12.5-μm-thick beryllium filter with ~80% x-ray transmission for the wavelengths of interest served as a visible-radiation shield. An additional covering of 80-μm-thick polyethylene (CH_2) with a transmission of ~70% was added to prevent punctures in the beryllium from target-debris impact.

III. RESULTS

A. Plasma composition

A sample streak spectrum is shown in Fig. 2. This particular spectrum was obtained at a nitrogen fill pressure of 1.5 Torr and off center (10 mm from one target), and was chosen in order to show a wide array of species. The wavelength region shown is rich in relatively intense $n=3$, $\Delta n=0$ spectral lines from N^+ and N^{2+} ions (N II and N III spectra). The wavelengths indicated have been compiled and tabulated by Striganov and Sventitskii [6]. These lines, and in particular the two highlighted by asterisks, namely N II 463.0543 nm and N III 463.416 nm, were used for the temperature and density diagnostics described below.

Also indicated in Fig. 2 are a pair of N V lines at 460.373-nm and 461.998-nm wavelengths. This species was only observed off center (i.e., not at the midpoint). Not shown and out of range of this spectrum is a N IV triplet with 347.871-nm, 348.299-nm, and 348.496-nm wavelengths, observed with a duration about twice that of the N V lines. These N IV and N V lines from N^{3+} and N^{4+} ions, respectively, are thought to be due to electron capture into excited states by the next higher ionic species and subsequent radiative decay, after being formed near the target and "frozen in" the expansion. According to modeling, they are not expected to be formed in the nitrogen expansion region itself [4]. These spectral lines peak near the target and then rapidly disappear in the blast wave region where the density increases (see Fig. 2), as would be expected from such an electron-ion collisional recombination process (rate proportional to N_e^3) at low temperatures. Hence, considering their origin, no localized diagnostics were attempted on these ionic species.

Also present at low intensities on some shots was an Al II spectral line at 466.3054-nm wavelength from Al^+ ions. This species was observed to always arrive late and probably originated in boiled-off debris traveling relatively slowly from the target surface. No Al III spectral lines were observed.

B. Blast-wave-region plasma parameters

1. Electron density

The electron density was determined from the half-width of the N II $3p\,^3P_2-2s\,^3P_2$ spectral line at 463.0543-nm wavelength, broadened by the Stark effect. Experimental data at lower densities have been compiled [7], and the width scales [8] linearly with electron density. From this we arrived at the scaling relation $\delta\lambda=0.33(N_e/10^{18})$ nm, where $\delta\lambda$ is the full width at half intensity and N_e is measured in units of cm^{-3}. An uncertainty of $\pm 30\%$ is expected from the compiled data. For an electron density of 1×10^{18} cm^{-3}, a linewidth of 0.33 nm greatly exceeds the instrumental resolution. The Doppler linewidth is estimated to be $\sim$0.02 nm for the $\sim$4 eV temperature reported below, i.e., negligibly small.

Measured electron densities are plotted versus time (measured from target irradiation) in Figs. 3 and 4 for nitrogen pressures of 1.5 and 5 Torr, respectively. Referring to Fig. 1, the three curves in each of Figs. 3 and 4 represent (a) dual colliding blast waves viewed at the midpoint between the target, (b) a single blast wave, also viewed at the midpoint, and (c) dual interacting blast waves viewed away from the collisional midpoint at $\frac{1}{4}$ the target separation distance, i.e., 7.5 mm from the target.

Considering first the midpoint viewing data, it is observed in Fig. 3 for a nitrogen fill pressure of 1.5 Torr that the peak electron density is 1.6 times larger with two colliding plasmas (a) than for one plasma (b). This is not apparent, however, in Fig. 4 at a higher fill pressure of 5 Torr, where there is no enhancement of the peak electron density by the collision. Furthermore, at late times (>1 μsec) it can be seen in Fig. 4 that the on-axis electron density is sustained at a level ≥ 2 times higher for colliding blast waves (a) compared to the single-plasma case (b). (This is most likely also present at the lower pressure in Fig. 3 but was not observable at such late times.) Finally, for the 5-Torr case shown in Fig. 4, it is noted that the electron density measured spectroscopically is in excellent agreement with that obtained from interferometry [5] for one dual-plasma shot.

For the dual-plasma, off-center (c)-type curves in Figs. 3 and 4 there are two peaks, and the second one is greater by 1.3 to 1.4 times. The first peak occurs earlier than for (a) and (b) because of the closer proximity to one target. For the shots shown in Fig. 4, the total distance of travel from the closer target to the viewing position (5 mm to the front) was 9 mm, and the first peak occurred at 0.26 μsec, for a mean velocity of 35 mm/μsec. The second and stronger peak arrives at 0.56 μsec after target irradiation with a velocity of 41 mm/μsec, whether it originated at the farther target or as a wave from the nearer target reflected by the second plasma or regenerated after the collision at the midpoint (the total distances are approximately the same). In either case there appears to be less attenuation in velocity for the second blast wave to reach the viewing point after traveling through a preheated plasma (in one direction or the other), compared to a $R^{-3/2}$ attenuation with distance R from the source for transport through a cold gas.

Plotted in Fig. 5 for comparison is the increased electron density for a 10-Torr nitrogen fill pressure for two dual-colliding-plasma type-(a) shots. A complete comparison with types (b) and (c) shots was not possible because of the low intensity of N II lines and the virtual absence of N III lines from a single target at this pressure. This figure is useful in showing the reproducibility obtainable for two shots obtained at nearly identical conditions.

Notice in Figs. 3–5 that the peak electron density is in the range of 10^{18} cm^{-3} and rises with increasing fill pressure, as might be expected. For comparison at different pressures, the experimental uncertainty in determining the relative electron density from measured linewidths is estimated to be $\pm 15\%$ and is indicated in Fig. 5. The uncertainty in the absolute values for the electron density is estimated to be $\pm 33\%$. These uncertainties are not expected to affect the overall differences in features found and discussed herein, only in the absolute values deduced. Some peak values for electron density are included in Table I.

2. Electron temperature

The electron temperature in the nitrogen plasma can be obtained from the intensity ratio between spectral lines of two different ionization stages [see Eq. (13-4) of Ref. [8]]. In the present case the two ionic species are N^+ and N^{2+} and the corresponding N II and N III spectral lines used are for transitions and wavelengths of $3p\,^3P_2-2s\,^3P_2$ at 463.0543 nm and $3d\,^2D_{3/2}-2p\,^2P_{1/2}$ at 463.416 nm, respectively (indicated by asterisks in Fig. 2). The N III to N II line intensity ratio scales as $(T_e^{3/2}/N_e)\exp(-41.3/T_e)$ in this case; i.e., is a very sensitive function of the electron temperature.

TABLE I. Peak parameters in the blast-wave region at the midpoint between targets, from time-resolved visible spectroscopy, and for single- and dual-blast waves.

	$N_e(10^{18}$ cm$^{-3})$[a]		T_e (eV)[b]		$\langle v \rangle$ (mm/μsec)[c]	
P (Torr)	Single	Dual	Single	Dual	Single	Dual
1.5	0.35	0.56	3.85	4.75	45	58
5	1.2	1.25	4.4	4.5	28	29

[a]N_e accuracy = ±15% relative, ±33% absolute.
[b]T_e accuracy = ±2% relative, ±10% absolute.
[c]Average velocity $\langle v \rangle$ obtained from 15.8-mm distance and time of peak N_e signal.

Wavelength-integrated line-intensity ratios yield absolute electron temperatures in the range of $kT_e = 3.5$–4.5 eV for all fill pressures and blast-wave conditions, at the times at which the temperatures are maximum. In obtaining these results, we used measured values for N_e at the same points in time. Such temperatures are reasonable for the appearance of spectral lines from singly and doubly ionized atoms. Some peak values for electron temperature are included in Table I.

Because the line-intensity ratio is a sensitive function of temperature, an estimated error of ±15% in performing the measurements, coupled with a similar error in measuring N_e, reflects as only a ±2% uncertainty in the relative temperature. This is important when comparing ratios of temperatures for different blast-wave cases such as (a) and (b) to (c) above and for different nitrogen pressures, and is shown in Fig. 7 as error flags on one curve. This is not the precision of the absolute temperature measurement, however, which is discussed below.

The validity of this method of determining the electron temperature depends on the assumption that the population in the higher-lying $n=3$ level in the N^+ ion is in partial local thermodynamic equilibrium (LTE) with the population of the ground state of the N^{2+} ions, as defined by Eq. (6-55) of Ref. [8]. For $kT=4$ eV, this LTE condition is achieved when the electron density exceeds 2×10^{16} cm^{-3}, which is clearly satisfied for this experiment. More restrictive is the requirement that the population of the upper level for the N III spectral line in the N^{2+} ion be in complete LTE with its own ground state. According to Eq. (6-60) and the discussion following Eq. (6-64) in Ref. [8], such complete LTE is achieved when the electron density exceeds 7×10^{17} cm^{-3} for the present case. This would be valid for the higher densities at a fill pressures of 5 and 10 Torr, according to Figs. 4 and 5. However, for a pressure of 1.5 Torr and for lower densities at all fill pressures, complete LTE may not exist. Hence, the line-intensity ratio formula may be differ by as much as a factor of 2 because of variations in the N^{2+} upper level population. Added to this is the effect of an uncertainty in the absolute value of the electron density of ±33%, discussed above. This reflects as only a ±3% uncertainty in the temperature. Hence, the overall uncertainty in the absolute electron temperature due to measurement errors, deviations from LTE, and electron density uncertainties is expected to be approximately ±10%. This is indicated for the data in Table I.

The measured electron temperature values are plotted versus time in Figs. 6 and 7 for nitrogen fill pressures of 1.5 and 5 Torr, respectively, and for the same shots, views, and electron densities shown in Figs. 3 and 4. No electron temperatures were obtainable at 10-Torr nitrogen fill pressure, because the N III spectral lines were unobservable. Excellent shot-to-shot reproducibility in temperature was obtained, similar to that for the electron density. From Fig. 6, the peak temperature measured on-axis is higher by ~24% for a dual-plasma shot than for a single plasma, for a nitrogen fill pressure of 1.5 Torr. Also, as for the electron density, there apparently is a less dramatic difference in (extrapolated) peak temperatures at early times for the higher-pressure case shown in Fig. 7. No sustained increase in electron temperature at late times at 5 Torr is apparent in Fig. 7, even though this was the case for the electron density as discussed above.

For the type (c) off-axis dual-plasma shots in Figs. 6 and 7, again, as for N_e, there are two peaks. However, in this case the temperatures are approximately equal, once again reflecting the lack of sustained increased heating after blast-wave collision at late times. Otherwise the data support the conclusions reached above.

C. Target region plasma parameters

1. Electron density

A microdensitometer tracing of a typical x-ray spectrum of an aluminum target obtained near a target surface is shown in Fig. 8. The dominant spectral lines are the n-to-1 (n being the principal quantum number), K-series Stark-broadened Al XII and Al XIII resonance series of heliumlike and hydrogenic Al^{11+} and Al^{12+} ions, respectively, as indicated.

A value for the electron density in the aluminum plasma can be obtained from the merging of these lines at large principal quantum numbers n. To deduce the electron density (N_e), which is responsible for the Stark broadening, we use the Inglis-Teller relation [9] in the version given in Eq. (5-46) of Ref. [8].

From a careful analysis of spectra such as depicted in Fig. 8, we estimate that the 7–1 and 8–1 transitions of the heliumlike Al^{11+} ion begin to merge with the continuum, yielding electron densities of $N_e = 12\times10^{20}$ cm^{-3} and 4.3×10^{20} cm^{-3}, respectively, for an average value of $N_e = 8\times10^{20}$ cm^{-3}, within ±50%. This will be used in the next section in determining the electron temperature by a sensitive method that does not reflect this large an uncertainty. This mean value is also included in Table II.

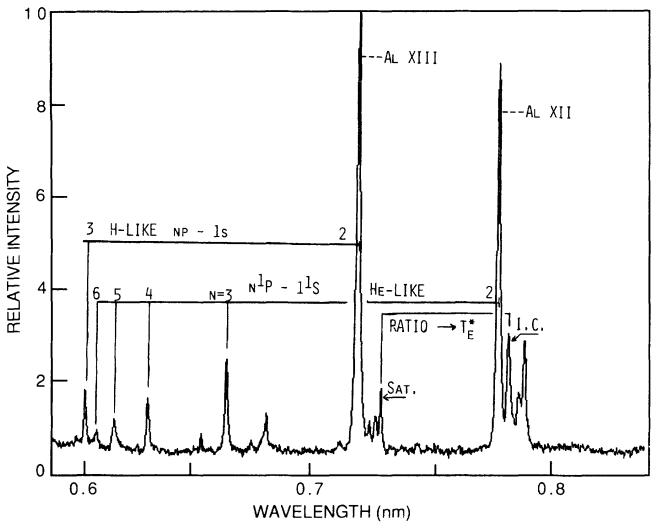

FIG. 8. Microdensitometer tracing of an x-ray spectrum taken at an aluminum target showing the resonance lines of H- and He-like ions, including the intercombination (I.C.) and satellite (Sat.) lines.

Another effect that obliterates high-level lines is a lowering of the ionization potential in a plasma environment [8]. An estimate of this effect shows that the electron density required to submerge the $n=8$ level is 4×10^{22} cm^{-3}, which is much higher than critical (10^{21} cm^{-3}) for the laser used. Hence, this effect is negligible for our conditions.

2. *Electron temperature*

We used two methods of determining the electron temperature in the recombining plasma formed near the aluminum targets from the soft x-ray emission, namely, (a) the relative population densities of high-n energy levels, and (b) intercombination-to-satellite line-intensity ratios. These will be discussed in sequence.

For plasmas in local thermodynamic equilibrium between excited states, the reduced population $N(n)/g(n)$ of an excited ionic state of principal quantum number n and statistical weight $g(n)$ follows a Boltzmann distribution; i.e., it is proportional to $\exp[-E(n)/kT_e]$, where $E(n)$ is the excitation energy measured from the ground state. Hence, $\ln[N(n)/g(n)]$ is linear in $E(n)$ with a slope determined by kT_e, the electron thermal energy. It is also linear with $\chi(n)$, the ionization potential of level n, because $E(n)+\chi(n)$ equals the ionization energy measured from the ground state. Following these arguments, the electron temperature is conventionally [10] obtained by plotting $\log_{10}[N(n)/g(n)]$ vs $\chi(n)$ and determining T_e from the slope, as shown in Fig. 9 described below.

Referring again to the typical spectrum shown in Fig. 8, we began by measuring the relative photographic densities of the spectral lines in the $n-1$ resonance series of heliumlike Al^{11+}. This photographic density is linear with exposure for Kodak DEF x-ray film for density values less than unity [11]. Both the film sensitivity and crystal efficiency are relatively constant over the narrow spectral range between compared lines. Such high-n lines do not have significant self-absorption, i.e., they can be considered to be optically thin to their own radiation. After minor corrections for variations in window transmissions, the relative line intensities were converted to relative reduced upper-state densities $N(n)/g(n)$, using known oscillator strengths [12].

The logarithm of this ratio is plotted versus $\chi(n)$ for a typical shot in Fig. 9, at a nitrogen fill pressure of 5 Torr. The slope of the line fitted to $n=5$ and 6 data points represents a best fit for $kT_e=165$ eV in this case. Lower levels ($n<5$) have progressively reduced intensities and effective densities because of self-absorption [10]. Data for $n=7$ are not available because of a blending with an overlapping 3-2 Balmer-α transition in hydrogenic Al^{12+}, as seen in Fig. 8. For $n>8$, the lines are too weak in intensity and blended with the continuum to be useful.

Notice in Fig. 9 that $N(3)/g(3)$ is significantly less than $N(4)/g(4)$, so that a line through these two points would yield a negative temperature. Hence, a population-density inversion exists, leading to possible x-ray lasing at a wavelength of 12 nm in this case. This is a typical phenomenon observed in all shots here and previously [13–17]. In a similar plot under near-vacuum conditions (0.054 Torr), the population-density inversion was

TABLE II. Average plasma parameters in the target vicinity, from time-integrated x-ray spectroscopy on Al-target plasmas.

$N_e=8\times10^{20}(\pm50\%)$ cm^{-3}
T_e(a)=210 eV (±30%) from high-n series line intensities
T_e(b)=235 eV (±20%) from intercombination/satellite line ratios
$\langle T_e\rangle$=225 eV average for methods (a) and (b)

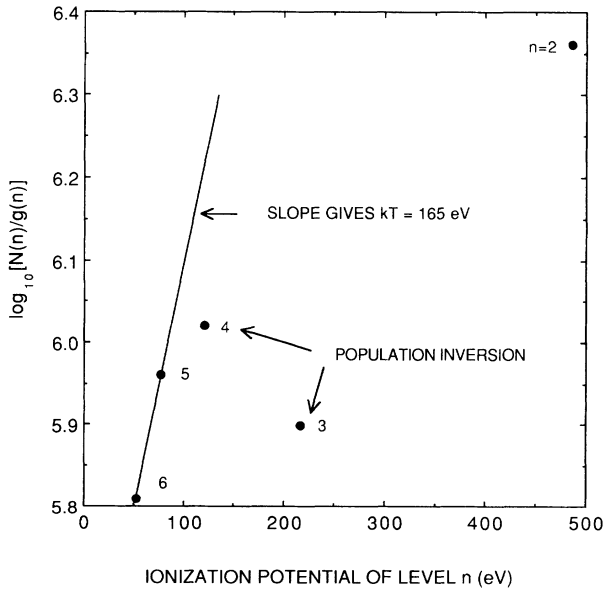

FIG. 9. Reduced upper-state densities vs ionization potential for an excited level n, where a fit at high n yields the plasma electron temperature near a target. Also shown is a population density inversion between $n=4$ and 3 levels. The nitrogen fill pressure is 5 Torr.

found to be much less. This implies that the presence of the gas enhances the inversion, either by increased cooling and collisional recombination [13,15,16] or by charge transfer [14,16,17].

A total of 16 shots analyzed yields an electron temperature using this method varying from 100 to 300 eV, with an average value of 210 eV. An uncertainty of ±30% is estimated. These results are included in the summary below, including Table II, along with those from method (b) to be described next.

Another (b) very sensitive temperature diagnostic is the ratio of relative intensities between the heliumlike Al XII $2p\ ^3P-1s\ ^1S$ intercombination line (I.C. in Fig. 8) and the heliumlike $2s2p$-$1s2s$ or $2p^2$-$1s2p$ doubly excited transitions (blended here), which are satellites (Sat. in Fig. 8) to the hydrogenic Al XIII $2p$-$1s$ Lyman-α transition. All of these transitions produce optically thin lines with negligible self-absorption, which is a great advantage over other resonance-line-ratio techniques.

Assuming that the $2p\ ^3P$ level is populated by recombination and is in Saha equilibrium with the continuum and the hydrogenic $1s\ ^1S$ ground state, the population density ratio between these two energy levels is known. The doubly excited state can be assumed to be populated by dielectronic capture, also from the $1s$ hydrogenic ground state. Hence, in the ratio of intensities I(IC)/I(Sat) the $1s$-state density cancels, and the temperature dependence in the relative line-intensity ratios for I.C. and Sat. upper levels is mainly exponential, with a weak residual electron-density dependence. Such an analysis has been completed by Fujimoto and colleagues [18]. The sensitivity of the intensity ratio to temperature is very strong, making the measurement quite accurate.

Once again, as described above, the relative line intensities between these two lines were measured on each shot, and the ratios were used to obtain a second value for the electron temperature. The results, included in Table II for the 16 shots analyzed, varied from 200 to 260 eV for an average value of 235 eV. The uncertainty in this value is estimated to be ±20%. The average temperature obtained by this (b) "ratio" method is slightly larger than for the "slope" method described as (a) above, but well within expected uncertainties of both methods.

The electron temperatures derived from analyzing data from many shots is plotted in Fig. 10 versus laser energy. The #1 and #2 designations refer to particular laser beams. There is an indication of a peak temperature in the vicinity of 220–260 J laser energy. If this overall average peak is indeed valid, it probably derives from variations in coupling of the laser energy to the target. The average temperatures are given in the figure and in Table II, along with the electron density. Higher peak temperatures may be present and not detected because of the integrations performed in the measurements; future numerical simulation of the conditions may predict such early-time enhancements.

IV. SUMMARY AND CONCLUSIONS

The plasma data obtained from visible and x-ray spectral measurements and analyses are collected in Tables I and II. The time history of the density and temperature in the regions of the colliding blast waves as well as the initial conditions at the target, respectively, should be useful for comparison with detailed modeling.

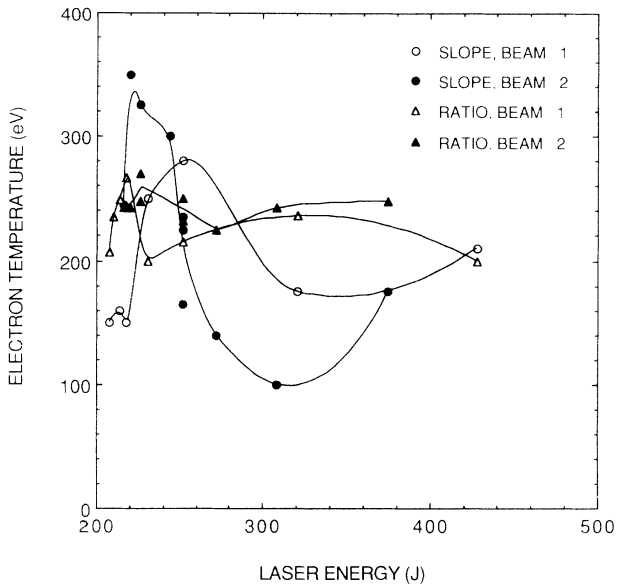

FIG. 10. Electron temperature near target surface vs laser energy from both "slope" and "ratio" measurements and for two targets, #1 and #2 (see Fig. 1). A possible maximum at low energies is apparent.

It was not possible to distinguish between a transmitted and a reflected (or regenerated) blast wave producing the second peak in density observed in off-center viewing. Most likely it is the latter, because the mean free paths are extremely short at the measured conditions. Future numerical simulations, based on these diagnostics, could shed light on such interpretations. Similarly, gated images of the plasma were inconclusive as to the degree of penetration and regeneration. The higher density measured at the second peak compared to that for the first represents the partial after-effect of the collision at midpoint, probably along with some reflection or regeneration. These conclusions are supported by spectroscopic data obtained on other shots at the same pressure and at other pressures. While it is inconclusive from the present measurements as to what degree the colliding blast waves interpenetrate and reflect or reform after collision, it can be concluded from the arrival times for the approaching and postinteraction blast waves that the average velocity is higher in traversing a region of plasma formed by a preceding blast wave than for transport through a cold gas.

ACKNOWLEDGMENTS

The technical assistance of J. L. Ford, N. E. Nocerino, and L. F. Daniels is acknowledged with appreciation. The authors are also grateful to C. A. Brown for useful suggestions concerning the analyses and to J. R. Fuhr of the NIST Center for Atomic Data for informing one of us (R.C.E.) of the oscillator strengths in Ref. [12]. This research was supported by the Office of Naval Research.

[1] B. H. Ripin, A. W. Ali, H. R. Griem, J. Grun, S. T. Kacenjar, C. K. Manka, E. A. McLean, A. N. Mostovych, S. P. Obenschain, and J. A. Stamper, in *Laser Interactions and Related Plasma Phenomena,* edited by G. Miley and H. Hora (Plenum, New York, 1986), Vol. 7, pp. 857–877.
[2] R. C. Elton, Naval Research Laboratory Report No. 5967, 1963, p. 8 (unpublished).
[3] R. C. Elton, J. Resnick, D.-M. Billings, C. K. Manka, J. Grun, and H. R. Griem, Bull. Am. Phys Soc. **36**, 2488 (1991).
[4] J. J. MacFarlane, G. A. Moses, and R. R. Peterson, Phys. Fluids B **3**, 635 (1989).
[5] J. A. Stamper (private communication).
[6] A. R. Striganov and N. S. Sventitskii, *Tables of Spectral Lines of Neutral and Ionized Atoms* (Plenum, New York, 1968).
[7] N. Konjevic and W. L. Wiese, J. Phys. Chem. Ref. Data **5**, 299 (1976); **19**, 1362 (1990).
[8] H. R. Griem, *Plasma Spectroscopy* (McGraw-Hill, New York, 1964).
[9] D. R. Inglis and E. Teller, Astrophys. J. **90**, 439 (1939).
[10] F. E. Irons and N. J. Peacock, J. Phys. B **7**, 2084 (1974).
[11] P. D. Rockett *et al.*, Appl. Opt. **24**, 2536 (1985).
[12] F. Khan, G. S. Khandelwal, and J. W. Wilson, Astrophys. J. **329**, 493 (1988).
[13] V. A. Bhagavatula and B. Ya'akobi, Opt. Commun. **24**, 331 (1978).
[14] R. C. Elton, T. N. Lee, R. H. Dixon, J. D. Hedden, and J. F. Seely, in *Laser Interaction and Related Plasma Phenomena, Vol. 5,* edited by H. J. Schwarz, H. Hora, M. Lubin, and B. Ya'akobi (Plenum, New York, 1981).
[15] V. A. Boiko, *et al.*, Kvant Elektron (Moscow) **11**, 1657 (1984) [Sov. J. Quantum Electron. **14**, 1113 (1984)].
[16] R. C. Elton, *X-Ray Lasers* (Academic, San Diego, 1990).
[17] R. H. Dixon and R. C. Elton, Phys. Rev. Lett. **38**, 1072 (1978); R. H. Dixon, J. F. Seely, and R. C. Elton, *ibid.* **40**, 122 (1978).
[18] T. Fujimoto, N. Yamaguchi, J. Mizui, T. Kato, and J. Fujita, J. Phys. D **14**, 439 (1981).

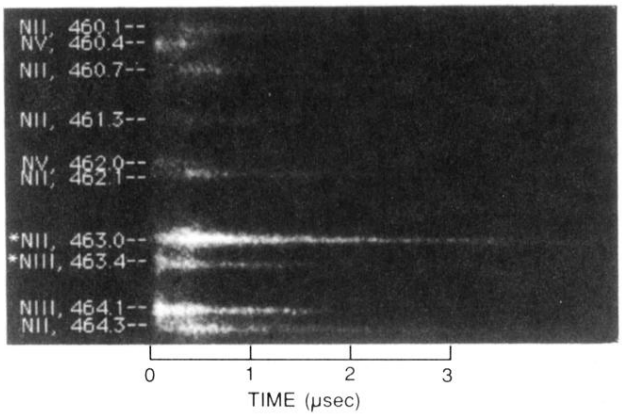

FIG. 2. Sample visible spectrum for the same dual-plasma shot as analyzed in Fig. 3, case (c), viewing off-center at 7.5 mm from the nearer target. N II spectral lines originate from N^+ nitrogen ions, etc. The wavelengths are indicated in nanometers. Asterisks denote two major lines analyzed for electron density and temperature. Time is measured here from the start of the spectral luminosity, not from that of target irradiation.